Electroanalytical Measurements of Lanthanum (III) Chloride in Molten Calcium Chloride and Molten Calcium Chloride and Lithium Chloride

Mark Schvaneveldt[a*], Ranon Fuller[a], Devin Rappleye[a]
[a]*Department of Chemical Engineering, Ira A. Fulton College of Engineering, Brigham Young University, Provo, UT, 84602, USA*

Abstract
Cyclic voltammetry (CV), square wave voltammetry (SWV) and other electroanalytical methods have been applied to molten chloride salts to study metal ion behavior. These studies have been useful for understanding and optimizing the electrowinning of metals. Notable ions that have been studied are rare earth and actinide metal ions in LiCl-KCl salts. However, the behavior of lanthanum (La^{3+}) ions in some molten chlorides or chloride mixtures (e.g., $CaCl_2$) has not been studied. CV experiments were conducted to evaluate La^{3+} behavior in $CaCl_2$-LiCl and $CaCl_2$ and were compared to La^{3+} behavior in LiCl-KCl and $CaCl_2$-NaCl eutectics from other studies. The electrochemical reaction was checked for reversible, quasi-reversible, and irreversible transitions in scan rate by examining the relationship between the scan rate applied and the peak current and potential for La^{3+} reduction. Properties such as diffusion coefficient (D_o) and electrons exchanged (n) were calculated from data. The electrochemical setup was also checked for radial diffusion based on the calculated La^{3+} diffusion coefficient and electrode radius, which led to the observation that natural convection possibly affected the La^{3+} reduction peak at low scan rates. For more accurate electroanalytical measurements of La^{3+} reduction, CV curves with and without $LaCl_3$ added to $CaCl_2$ and $CaCl_2$-LiCl were compared to establish baselines for the La^{3+} reduction peak. The impact of resistance (IR) compensation on the La^{3+} reduction peak was also explored. Techniques and practices that improved electroanalytical measurements include placing the electrolytic cell in a Faraday cage, distancing electrodes from the heating coils, and melting the chlorides twice prior to measurements.

Keywords
rare earth; lanthanum; molten salt; cyclic voltammetry; reversibility; diffusion coefficient

1. Introduction

Rare earths have been identified as critical materials by multiple nations [1–4] because of their strategic importance to security and the economy [4,5]. A major challenge to the processing of rare earth minerals is the presence of uranium and thorium [6,7], which are difficult to separate from rare earth elements [8] due to similar properties [9] and are strictly regulated elements. Hence, a dry method to extract U and Th that minimizes the volume of radiological waste and removes troublesome impurities is desirable. Chloride volatility has previously been investigated as a potential dry method to remove impurities from rare earths [10–12]. Chloride volatility exploits the low vapor pressures of rare earth chlorides (<<1 Pa up to 800°C) by volatilizing and sweeping away impurities under a flowing gas. Recently, it was demonstrated that U could be removed from $CeCl_3$, if the reacting chlorine gas contained very little (<1 ppm) moisture and oxygen [12]. If rare earth metals are desired, an additional challenge remains after purification via chloride volatility, to reduce the purified chlorides. Metallothermic reduction with calcium is a proven approach, but requires extensive purification of the reductant to limit the introduction of impurities [13,14]. The reduction of molten rare earth chlorides via electrolysis (e.g., electrowinning) removes the need for high purity reductants and is a common method used commercially [14]. Most of the rare earth chlorides have high melting points (>700°C). Hence, a common practice is to mix the rare earth chlorides with a suitable alkali and/or alkaline earth metal chloride to reduce the operating temperature for electrolysis by the formation of

* Corresponding author at: Department of Chemical Engineering, Ira A. Fulton College of Engineering, Brigham Young University, Provo, UT, 84602, USA
Email addresses: mschvane@byu.edu

 https://doi.org/10.1016/j.jelechem.2022.116442

eutectics. In the context of chloride volatility, electrowinning of rare earth chlorides is attractive because of its potential to simultaneously reduce rare earth chlorides to metal and generate high-purity chlorine gas.

In this study, lanthanum was selected as the representative rare earth in the electrowinning process, and its reduction was analyzed. The analysis of the oxidation of chlorine ions to chlorine gas will be presented in another publication. Rare earth metals, including La, have been electrolyzed from fused chloride melts starting in 1875 with subsequent investigations improving the metal purity and current efficiencies [14,15]. La has been studied in the LiCl-KCl [16–26], $CaCl_2$-NaCl [22,27,28], and NaCl-KCl [22,29–31] systems. Systems containing $CaCl_2$ are particularly attractive in the application to the chloride volatility purification process due to the low vapor pressure of $CaCl_2$, which will minimize contamination of the generated chlorine gas. No publications were found on the electrochemical behavior of La in pure $CaCl_2$ and $CaCl_2$-LiCl. Hence, this work focused on studying the reduction of $LaCl_3$ in these two melts.

In this study, cyclic voltammetry (CV) experiments were conducted to evaluate La^{3+} behavior in $CaCl_2$-LiCl and $CaCl_2$. The properties observed for dilute La (<5 wt%) in $CaCl_2$-LiCl and $CaCl_2$ were compared to the previously published results for La in $CaCl_2$-NaCl and LiCl-KCl. In addition to the unique base melts, these experiments were conducted in higher-temperature environments, exceeding that in other studies [16–19,21–25,27] by approximately 300-400°C. Also, this study utilized a square wave voltammetry (SWV) model developed and validated for soluble-insoluble reaction to improve upon the previous approach [21,22,24,32] of determining the number of electrons exchanged (n) for La studies in molten salts. The unique base melts, increased operating temperatures, improved property calculations, and thorough experimental methods provide valuable additional information into La behavior in molten salts.

2. Experimental

All electrochemical experiments were performed in a glovebox (LC Technology) under an argon atmosphere. The experiments were conducted in a split tube furnace (MTI, OTF-1200X-S-NT-LD), which melted chlorides at 690-825°C (see Figures 1 and 2). The furnace was supported vertically by a custom stand. The furnace features an 8” heating zone and a programmable controller. A nickel tube (alloy 200, 2” OD, .065” width, 12” length) was inserted into the tube furnace to shield the furnace interior from molten salt spillage and vapors (see Figures 1 and 2). The Ni tube also served as a faraday cage to shield the experiments from electromagnetic induction from the coiled heating element wires in the furnace. The bottom of the Ni tube was wrapped in coiled copper or tungsten wire, which was grounded. The tube furnace and Ni tube were initially heated with exposure to oxygen, which oxidized the tube. The nickel oxide layer provided a protective coating during experiments.

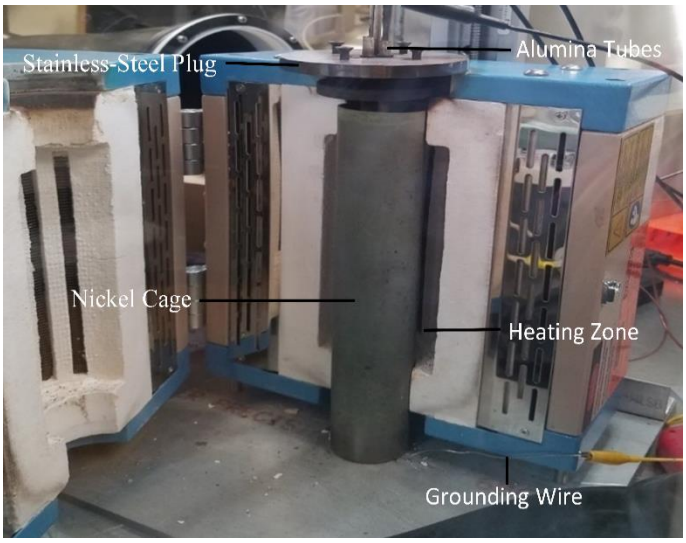

Figure 1. Picture of electrochemical cell setup featuring the tube furnace, nickel faraday cage, stainless steel plug, and grounding wire.

https://doi.org/10.1016/j.jelechem.2022.116442

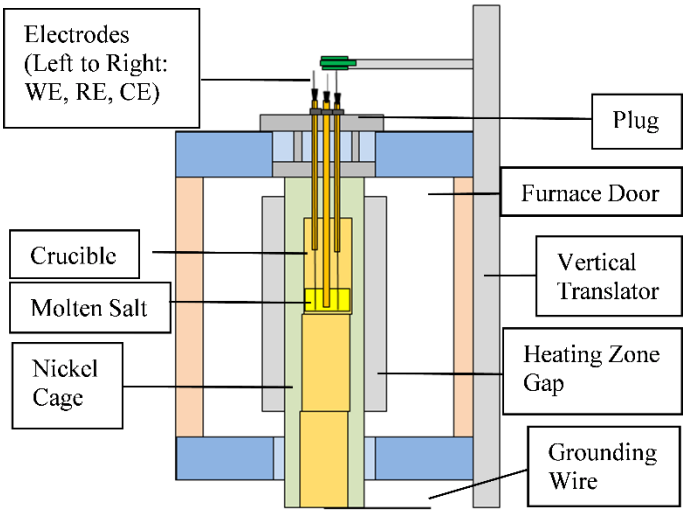

Figure 2. Sketch of electrochemical cell setup featuring tube furnace interior, electrodes, and vertical translator.

2.1. Electrodes

The opening to the tube furnace was capped by a custom-built, stainless-steel plug (see Figures 1 and 2). The plug consisted of two circular plates joined by metal screws. Holes drilled through the plug positioned the electrodes as the electrodes were lowered into the molten salt. The holes' placement prevented noise that results from the electrodes being positioned too close to the heating coils of the tube furnace. The holes' placement also prevented shorting that results from misaligned electrodes contacting. The working electrode (WE) was lowered via a graduated vertical translator (Velmex, Part #A2509P10-S2.5 CO68120) with 0.025 mm (0.001") precision mounted to the tube furnace's stand (see Figure 2).

A potentiostat (Metrohm Autolab, Model PGSTAT302N) supplied power to the electrodes from outside the glovebox. The potentiostat connected to the electrodes through binding posts on the glovebox and through sleeved alligator clips with spade terminals. As the potential applied to the electrodes varied, the WE current response was recorded. Experiments were repeated at varying scan rates.

The WE was a 0.5mm tungsten wire (Alfa Aesar, 99.95%, stock no. 42233) or a 1.5mm tungsten rod (Alfa Aesar, 99.95%, stock no. 42233). The counter electrode (CE) was a coiled 0.5mm W wire or a 3.175mm W rod (Alfa Aesar, 99.95% metals basis, stock no. 10407). W rods were more reliable because of their rigidity which resulted in fewer shorts and easier depth measurements based on adhered salt. The adhering salt was measured post-experiment—to allow for complete electrode wetting—using a digital caliper (General Ultratech, ±0.1mm). The post-experiment depth measurements were corroborated with depth estimates based on vertical translator positioning. The depth of the WE was estimated using the vertical translator by lowering the WE until the CV current response at the electrode was stable (i.e., exceeded noise levels), indicating the electrode tip contacted the molten salt surface. Additional lowering of the WE past this point approximated the length of electrode immersed in salt.

The WE and CE were sheathed in alumina tubes (Advalue Technology, >99.6% Al_2O_3, 6.35 mm OD, ~100 mm height) (see Figures 1 and 2). The alumina tubes were positioned high enough to avoid contacting the molten salt while electrically insulating the electrodes from the stainless-steel plug. The alumina tubes were positioned in the stainless-steel plug by Viton O-rings (6.07x1.78mm) (see Figure 2).

2.2. Reference Electrode

The reference electrode (RE) was constructed from closed-ended mullite tubes (McDanel Ceramics, 60% Al_2O_3, 37.9% SiO_2, 11mm OD, 305mm length) or alumina tubes (Advalue Technology, >99.6% Al_2O_3, 12.7mm OD or 6.35mm OD, 305mm length). The 11mm OD mullite and 12.7mm OD alumina tubes were thinned near the closed

 https://doi.org/10.1016/j.jelechem.2022.116442

end with a tile saw, to improve ionic contact between the RE and bulk solution. However, the thinner walls of the 6.35 mm OD alumina tubes did not require additional thinning via tile saw. The electrical lead for the RE was a silver wire (Alfa Aesar, annealed wire, 99.9% metals basis). Approximately 380mm of wire was pushed through the RE into the RE salts to the bottom of the tube by gently shaking and tilting the tube 120°. Wire was re-used for newly prepared REs by cutting wire exposed to RE salt in used REs. The REs were capped with tapered rubber (EPDM) plugs. The RE was inserted into the stainless-steel plug and supported by a Viton O-ring. The RE tip was inserted into the crucible salt and suspended just above the bottom of the crucible. The RE salt melted for 30-60^{+} minutes prior to electrochemical measurements. The melting time assisted the 'impregnation' of ions across the ceramic membrane and established better ionic contact between the RE and crucible salt.

RE salt was approximately 5 mol% AgCl (Alfa Aesar, Premion®, 99.997% metals basis, stock no. 10857) in dried $CaCl_2$ (Alfa Aesar, Calcium chloride dihydrate, 99% min, stock no. 33296). The salt was weighed with a Precision Balance (Radwag, Model PS 3000.3Y, 1mg readability, 4mg linearity) alongside a workstation ionizer (SPI Westek, Model 94000). The ionizer prevented significant weight differences from static charges in a dry environment. The salt mass was verified by weighing the weight boats, closed-ended tubes, and funnel (borosilicate, long-stem) before and after the addition of each compound to the RE. The salt mass ranged from 1.57-1.61g in the 11mm and 12.7mm OD ceramic tubes and 0.77-0.82g in the 6.35mm OD alumina tubes.

2.3. Ceramics Preparation

The alumina crucibles (Advalue Technology, >99.6% Al_2O_3, 40mm OD, 95mm height) containing salt were placed inside the nickel tube and elevated within the tube furnace heating zone. The elevated crucibles were supported by stacked alumina crucibles. Some crucibles were cleaned and reused for some electrochemical experiments. The used crucibles were immersed in water under low heat until the salt contaminants—from prior experiments—dissolved. Then the crucibles were immersed in aqua regia solution—5 vol% 1:3 HNO_3 (Fisher Chemical, stock no. A200-500, 69-70% w/w) to HCl (Fisher Chemical, stock no. A144-500, 36.5-38% w/w) in distilled water. The solution was heated until it boiled and then kept under low heat for 30 minutes. The crucibles were removed and rinsed with water. Afterward, the crucibles were dried.

All ceramics were dried prior to experimentation. Ceramics were dried for 6-12 hours at 250°C in a vacuum furnace (Across International Vacuum, Model AT32e). The vacuum furnace features a cold trap (Model T40-UL) and a vacuum pump (Model SuperVac-11C). Nitrogen (Airgas, UHP200C) was added to this furnace after drying the ceramics under vacuum, to minimize moisture contamination from air. The ceramics were subsequently transferred to the glovebox and dried for 2 hours at 900°C.

2.4. Chloride Preparation

Chlorides were also dried prior to experiments based on thermogravimetric data in the literature [33–35]. The salts were dried in borosilicate bowls, which were placed in either the custom oven in the glovebox or the Across International Vacuum oven used for drying ceramics. However, $LaCl_3$ (Alfa Aesar, Lanthanum (III) chloride, ultra-dry, 99.9% [REO], stock no. 35702) was not dried prior to experimentation, save on one occasion after suspected air contamination from a glovebox leak. On this occasion it was dried by heating the salt up to 135°C for over 3 hours and 40 min, then held at 135°C for 24 hours. LiCl from Alfa Aesar (anhydrous, 99%, stock no. 10515) was dried at 185°C for 4 hours and from Fisher Chemical (≥98.5%, stock no. L121-500) was dried at 110°C for 3 hours, then at 186°C for 18 hours. $CaCl_2$ dihydrate was dried by holding the oven temperature (while under vacuum) at 200°C for 24 hours.

50.4-51.1g of dry chloride salts was added to the crucibles for each experiment. The salts were 0.49-1.02g $LaCl_3$ (depending on the experiment) with the remainder either $CaCl_2$ or a $CaCl_2$-LiCl (23 and 77 mol%, respectively) mixture. Like RE salt preparation, the mass of chlorides was verified through weighing the weight boats and crucibles before and after the addition of each compound. Mass was measured with the Radwag Precision balance alongside the SPI Westek workstation ionizer.

Post-experiment, the temperature of the molten salts was measured. The electrodes were removed, and a type-K thermocouple was inserted (Omega, KMQXL-125U-12) through the stainless-steel plug. The thermocouple was attached to a digital thermocouple temperature thermometer (Proster, Model JL:2183458, 1.5% accuracy, 0.1°C resolution). Salt samples were taken via stainless-steel threaded rods (2mm OD) and quartz capillary tubes (1.5mm ID) to verify chloride concentrations. The salt samples were assessed via ICP-MS.

Table 1 provides the material and experimental conditions for each of the reported CV tests.

 https://doi.org/10.1016/j.jelechem.2022.116442

Table 1
Reported CV Experiments with Associated Properties and Materials.

Test	Wt% $LaCl_3$	Solvent Matrix	Temp (°C)	IR Comp. (Ω)	WE		CE	RE		
					Metal	Surface Area (cm^2)		Ceramic	Metal	AgCl (mol%)
CV1	1	$CaCl_2$-LiCl	697.8	0.3	0.5mm W wire	0.49	0.5mm coiled W wire	Thinned Mullite	0.64mm Ag wire	5.27
CV2	1	$CaCl_2$-LiCl	802.7	0.3	0.5mm W wire	0.49	0.5mm coiled W wire	Thinned Mullite	0.64mm Ag wire	5.27
CV3	2.2	$CaCl_2$-LiCl	820.8	0.25	1.5mm W rod	0.21	3.175mm W rod	Alumina	0.64mm Ag wire	5.15
CV4	1.5	$CaCl_2$-LiCl	822.0	0.12	1.5mm W rod	0.62	3.175mm W rod	Alumina	0.64mm Ag wire	4.27
CV5	2	$CaCl_2$	794.5	0.3	0.5mm W wire	0.50	0.5mm coiled W wire	Alumina	1.2mm Ag wire	5.71
CV6	2.2	$CaCl_2$	823.1	0.1	1.5mm W rod	0.54	3.175mm W rod	Alumina	0.64mm Ag wire	4.93

3. Results and Discussion

3.1. $LaCl_3$ in $CaCl_2$-LiCl

A 'full window' CV for $LaCl_3$ in $CaCl_2$-LiCl is shown in Figure 3. In this and the CV curves that follow for this salt mixture, La is suspected to electrodeposit at B' prior to Ca likely reducing onto La at A". Thermodynamic calculations predict $CaCl_2$ has a more positive standard reduction potential than LiCl [36–39]. Furthermore, La has a high solubility for Ca according to the Ca-La phase diagram, which could result in a more positive deposition of Ca due to reduced activity of the metal [40]. The La-Li phase diagram shows little interaction [41]. After A", Ca and Li are co-deposited at A', as has been reported for LiCl-KCl-$CaCl_2$ [36,37] and LiCl-$CaCl_2$ [42] melts. As the potential increases following reduction, Ca and Li oxidize at A prior to La stripping at B. Note that at approximately 0.4V, material oxidizes gradually at C prior to a sharp rise in oxidation current at D. C is suspected to correspond to the electrode metal (W) oxidizing prior to the formation of Cl_2 at D from the chlorine ions in the molten salt. The lack of the associated reduction peaks for C and D indicates that the oxidation products escape from the salt, are unstable or are not electroactive. In the case of D, Cl_2 gas likely bubbles out of solution before it can be reduced. In the case of C, it is less certain since limited study of the anodic behavior of W in molten chloride salts has been performed. The +4 oxidation state has been identified as the lowest stable oxidation state of W in a molten chloride salt and an estimated standard reduction potential of -1.119 V vs Cl^-/Cl_2 has been estimated at 973 K in molten NaCl-CsCl salt [43]. The current begins to rise on the C feature at ~1 V more negative than D. Furthermore, the standard reduction potential (E^o) has been estimated to be -0.630 V and -0.394 V vs Cl_2/Cl^- at 973 K for gaseous WCl_4 and WCl_6 (boiling point: 620 K), respectively, based on thermochemical properties [38,44]. The spacing between C and D is approximately -0.5 V. In addition, dark blue material (the color characteristic of WCl_6) condensed onto the alumina sheaths housing the electrodes while conducting CV tests. Hence, it seems reasonable to assume that C is related to the formation of some tungsten chloride compound, which is likely gaseous or reacts with Cl_2 to form a gaseous product at CV1 test conditions (971 K).

 https://doi.org/10.1016/j.jelechem.2022.116442

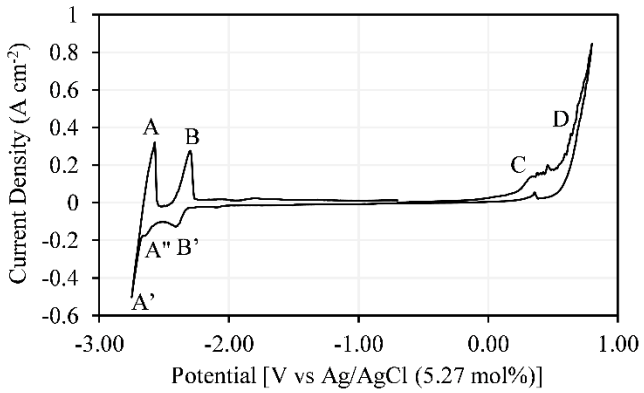

Figure 3. CV1 at 200 mV s^{-1} A/A': Ca and Li oxidation/reduction; A": Ca deposition onto La; B/B': La oxidation/reduction; C: W oxidation; D: Cl^- oxidation/Cl_2 formation.

The La reduction peak height and peak potential were evaluated from the baseline as a function of scan rate to determine diffusive and kinetic properties. In Figure 3, it appears that the baseline could potentially shift more negative during B'. However, overlaying the CV of $CaCl_2$-LiCl with $LaCl_3$ on the CV of pure $CaCl_2$-LiCl (see Figure 4) demonstrated that the background current is relatively constant where La reduction takes place (it decreased no more than 0.005A cm^{-2} per volt). This baseline is essentially 'flat' compared to the decrease in current density representing the reduction of La (see Figure 4). Assuming a 'flat' baseline for this salt system yielded D_o values comparable to those found in literature for La in similar salt systems [22,32,45]. Also note that immediately after the La oxidation peak, there is a ridge or 'shoulder', which may be due to the higher concentration of $LaCl_3$ (2.2 wt%). At higher concentrations, more negative current densities are generated during the electrodeposition of La. As a result, a thicker deposit of La metal forms. Upon oxidation, the underlying metal layers are delayed in oxidizing into the salt until the top layers have oxidized. Furthermore, if the solubility limit for $LaCl_3$ has been reached at the electrode-salt interface, then the underlying metal layers are delayed by the diffusion of La^{3+} ions away from the WE. For all CVs containing less than 1.5 wt% $LaCl_3$ no shoulder was observed. However, a conclusive explanation for the shoulder requires further investigation.

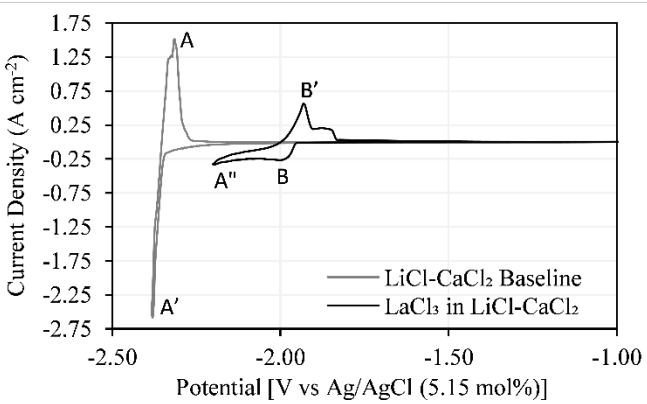

Figure 4. CV3 at 200 mV s^{-1} overlaid on CV of $CaCl_2$-LiCl, at 810°C at 200 mV s^{-1} with 0.25Ω resistance compensation (same electrodes except the WE area is 0.39cm^2). A/A': Ca and Li oxidation/reduction; A": Ca deposition onto La; B/B': La oxidation/reduction.

3.1.1. Scan Rate Relationships

According to Figures 5-7, there is a clear relationship between the CV scan rate and the La reduction peak height in the $CaCl_2$-LiCl salt matrix. As the scan rate increases, the peak height also increases. According to Figure 6, the

 https://doi.org/10.1016/j.jelechem.2022.116442

relationship between current response at the WE and scan rate is linear, even up to high scan rates (up to 2.5 V s^{-1}). For other salt systems, it is more typical to see linearity at low scan rates before transitioning to a separate linear trend at higher scan rates [46–49]. This more typical behavior illustrates the transition from electrochemical reversibility to irreversibility. Persistent linearity up to 2.5 V s^{-1} across multiple experiments suggests that the reduction of La^{3+} is electrochemically reversible up to 2.5 V s^{-1} at these elevated temperatures.

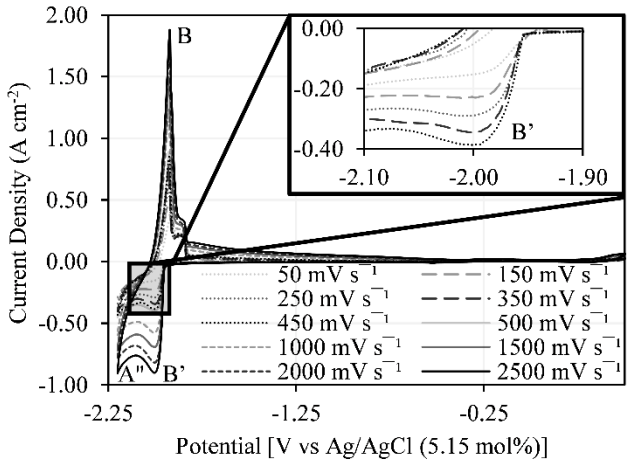

Figure 5. Cyclic voltammograms from CV3 at multiple scan rates. A": Ca deposition onto La; B/B': La oxidation/reduction.

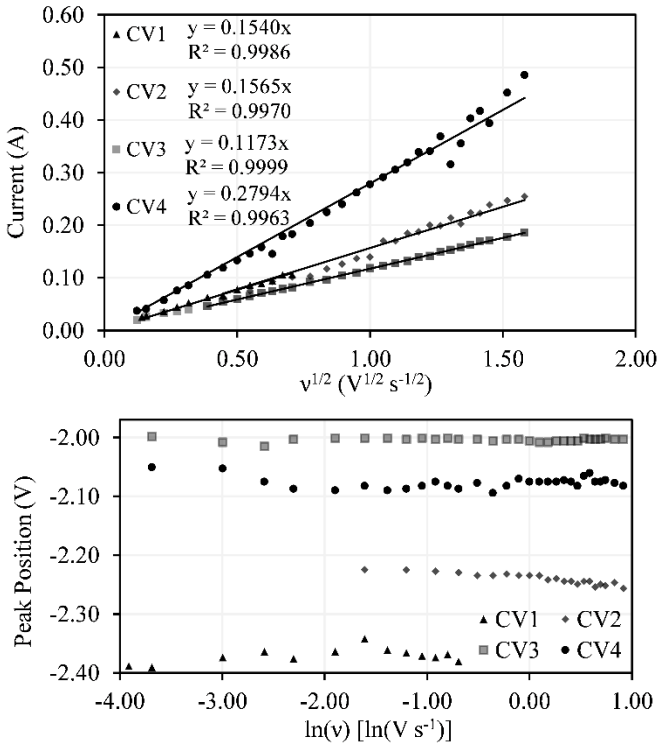

Figure 6. Plots of peak height with the square root of scan rate (top) and the trend of peak position with the natural log of scan rate (bottom) for all tests in $CaCl_2$-LiCl.

https://doi.org/10.1016/j.jelechem.2022.116442

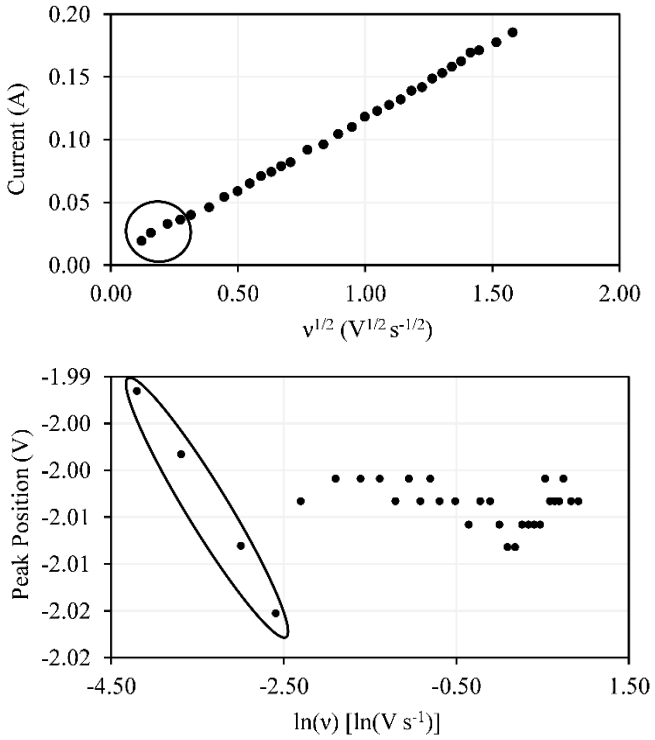

Figure 7. Peak Height versus square root of scan rate (top) and peak potential versus natural logarithm of scan rate (bottom) for CV3. Excluding circled data, peak potential does not have a definite trend with scan rate.

According to Figure 6, the potential of the La reduction peak position is consistently independent of scan rate. For typical salt systems illustrating a transition from reversibility to irreversibility, there is a dependence of reduction peak position on scan rate. This further illustrates that this salt system is reversible up to high scan rates.

A possible transition from reversibility in CV3 (see Figure 7) was considered but deemed conclusively negligible. At low scan rates (<100 mV s^{-1}), the La reduction peak heights and positions indicated a slight deviation in linearity and a dependence on scan rate respectively. However, the La reduction peak height and position were difficult to measure at those scan rates (see inset of Figure 5). The current density does not show a clear minimum. The peak heights and positions cannot be verified because the peaks cannot accurately be distinguished from the reduction of Ca. Hence, these estimations are inaccurate and cannot be used to conclude a transition from reversibility.

Excluding the data derived at low scan rates demonstrates a linear trend with respect to reduction peak height and an independent trend with respect to reduction peak potential. Therefore, data collected at low scan rates, with virtually indistinguishable peaks, were not accounted for in evaluating kinetic and mass transport information for La^{3+} in $CaCl_2$-LiCl (see Figures 6 and 7).

Semi-infinite linear diffusion was verified after demonstrating that Eq. (1) was satisfied for all scan rates [50–53]:

$$\frac{D_o \tau}{r^2} \leq 3 \times 10^{-3} \tag{1}$$

where

$$\tau = \frac{RT}{nFv} \tag{2}$$

https://doi.org/10.1016/j.jelechem.2022.116442

r is electrode radius (m) and D_o is the diffusion coefficient ($m^2\ s^{-1}$) calculated from the Berzins-Delahay equations (see Eqns. 3 and 4). If there was no error in measurement, and because semi-infinite linear diffusion was validated, La^{3+} transport at low scan rates in $CaCl_2$-LiCl is explained by natural convection rather than radial diffusion [50–53].

3.1.2. Berzins-Delahay Comparison

Relations derived by Berzins and Delahay [50] for soluble-insoluble systems were used to analyze the data for mass transport and kinetic properties:

$$I_p = 0.6105A\sqrt{\frac{(nF)^3 D_o \nu}{RT}}C \tag{3}$$

$$\Delta E_p = \left|E_p - E_{p/2}\right| = 0.774\frac{RT}{nF} \tag{4}$$

I_p is the reduction peak current (A), A is the surface area of the electrode immersed in electrolyte (cm^2), n is the number of electrons exchanged, D_o is the diffusion coefficient of the analyte ($cm^2\ s^{-1}$), ν is the scan rate ($V\ s^{-1}$), T is the temperature of the electrolyte (K), and C is the concentration of analyte ($mol\ cm^{-3}$). E_p and $E_{p/2}$ are the peak potential and peak potential at half height (V), respectively.

The Berzins-Delahay relations have been commonly used for determining the number of electrons exchanged for soluble-insoluble systems, particularly for rare earth and actinide studies [47,54–57]. The number of electrons exchanged, *n*, was calculated using Eq. (4) and the measured difference of the peak potential E_p and peak potential at half height $E_{p/2}$. This difference was calculated from the data via the software accompanying the potentiostat. Because La^{3+} is reduced, *n* is expected to be 3. However, *n* was 0.47-2.4, depending on the experiment and scan rate.

To investigate the discrepancy in *n*, the predicted shape for the reduction peak based on the Berzins-Delahay relations was plotted and overlaid with data in Figure 8. According to Figure 8, the reduction peak of La does not behave exactly as predicted by the Berzins-Delahay relations—the peak width for the data is consistently broader. The broader peaks likely result from deposition of La on a foreign substrate. Fatourus et al. performed computation simulations of metal deposition on foreign substrates, which showed underpotential deposition and broadening of the deposition wave [58]. This clearly demonstrates the need for improved relations for predicting the shape of reduction peaks for metal deposition on foreign substrates in molten salts.

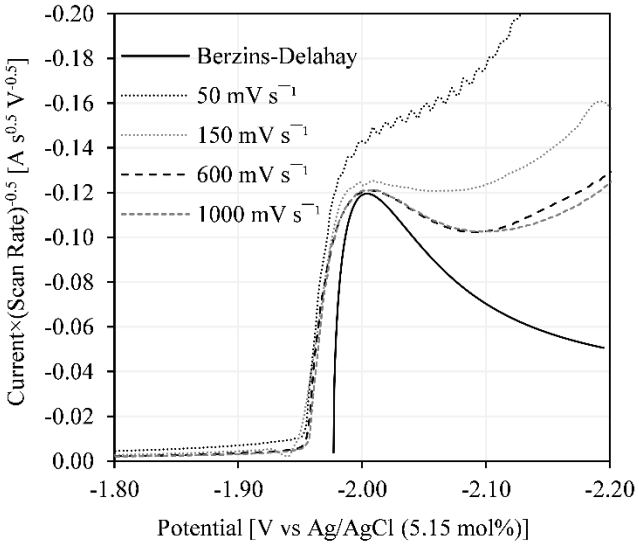

Figure 8. CV3 Overlay of Normalized Current and Predicted Berzins-Delahay Current.

https://doi.org/10.1016/j.jelechem.2022.116442

3.1.3. Square Wave Voltammetry

Square-wave voltammetry (SWV) was used to determine the number of electrons exchanged (*n*) using a step potential of 5 mV and pulse amplitude of 50 mV over a range of frequencies. Figure 9 shows the resulting SWV response at 15 Hz. This does not form the ideal bell curve typical of soluble-soluble reactions. This is partly due to the deposition of La onto a foreign substrate. The deposition of metal onto a foreign substrate was investigated and modeled by Fatouros and Krulic [59] and was further investigated and validated by Fuller et al. [60]. Fatouros and Krulic observed that the soluble-soluble model for the SWV peak width at half height ($W_{1/2}$) developed by Barker [61], Ramaley and Krause [62], and Aoki et al. [63], as shown below, is "only right by chance" [59] in determining *n* in a soluble-insoluble reaction.

$$W_{1/2} = 3.53\frac{RT}{nF} \tag{5}$$

Indeed, if Eq. (5) is applied to the peak width at half height observed (0.0362 V) in Figure 9, a *n* of 6.79 is calculated. Fatourus and Krulic developed a relation for the width of the back half of the peak at half height (w_2) [59]:

$$\mathcal{W}_2 = 0.37\chi^{-0.5} + 0.45\chi^{0.11} + (0.26 + 0.01\chi)\rho \tag{6}$$

where

$$\mathcal{W}_2 = \frac{w_2 nF}{RT} \tag{7}$$

$$\chi = \frac{C_{ox}^{*}\sqrt{D_{ox}\Delta t}}{\Gamma_1} \tag{8}$$

$$\rho = \frac{n^2F^2AR_uC_{ox}^{*}\sqrt{D_{ox}}}{RT\sqrt{\Delta t}} \tag{9}$$

Δt is the pulse time (s), Γ_1 is the monolayer density (mol cm^{-2}), and R_u is the uncompensated resistance (Ω). All other symbols retain their previously defined meanings. Eq. (6) is referred to as the 'F&K Full Model'. Applying the observed w_2 in Figure 9 and the conditions of the CV3 test, a *n* of 2.98 is calculated. An approximated *n* can be calculated using a simpler model proposed by Fuller et al. and assuming negligible uncompensated resistance [60].

$$w_2 = 0.9\frac{RT}{nF} \tag{10}$$

Eq. (10) predicts a *n* of 2.93. To ensure that a frequency of 15 Hz ($\Delta t^{1/2}$ = 0.183 s) is appropriate for determining the number of electrons exchanged using Eq. (10), w_2 was measured from SWV profiles over a range of frequencies. The w_2 values observed are plotted in Figure 10 along with w_2 values predicted by Eq. (6) (F&K Full Model) and Eq. (10) (Fuller Model). Eq. (10) shows that w_2 is independent of frequency. As illustrated in Figure 10, w_2 plateaus after $\Delta t^{1/2}$ = 0.1 s (50 Hz) confirming that the application of Eq. (10) is reasonable and a *n* close to 3 was not random chance.

 https://doi.org/10.1016/j.jelechem.2022.116442

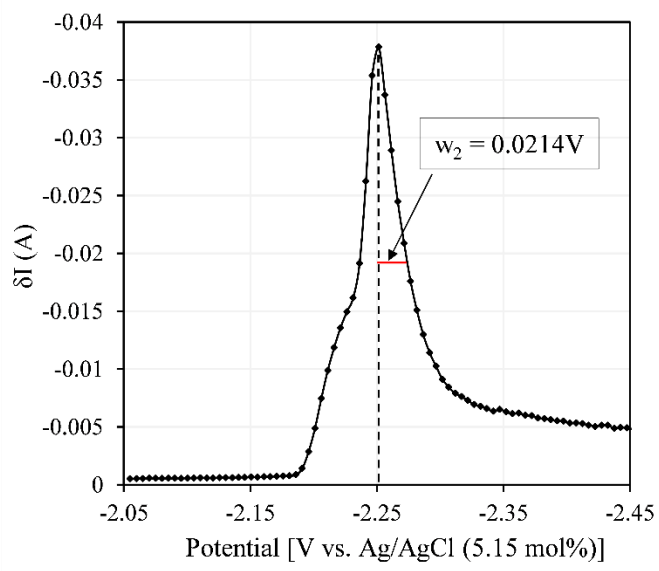

Figure 9. SWV profile for La deposition onto a W WE (area: 0.20 cm^2) at 15 Hz (step potential: 5 mV, pulse amplitude: 50 mV).

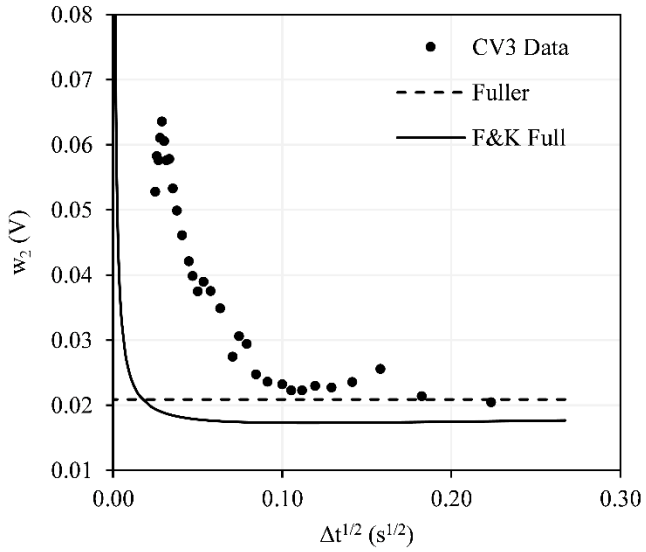

Figure 10. Values of w_2 for SWV measurements (step potential: 5 mV, pulse amplitude: 50 mV) over a range of frequencies for La deposition onto a W WE (area: 0.20 cm^2) with predicted values from models overlayed.

3.1.4. Diffusion Coefficients

D_o was determined for $LaCl_3$ in $CaCl_2$-LiCl, with varying temperatures and concentrations of $LaCl_3$ (see Table 2). The concentration of $LaCl_3$ (mol cm^{-3}) was found by assuming that the molten salt mixture was ideal and the volumes of $CaCl_2$, LiCl, and $LaCl_3$ were additive. The volume of the $CaCl_2$-LiCl mixture was determined through linear interpolation of data [64] and the volumes of $LaCl_3$ and $CaCl_2$ were determined through empirical relations [65,66]. Whenever ICP-MS was conducted for experiments to verify the concentration of $LaCl_3$ in the molten salts, this concentration was used to determine D_o. However, salt samples taken using quartz capillaries (CV1 and CV2) were very small (9.5-11 mg). ICP-MS analysis of these samples resulted in concentrations of $LaCl_3$ more than twice

 https://doi.org/10.1016/j.jelechem.2022.116442

than expected based on weighed salt masses. This may be due to non-representative sampling of the molten salt. In these cases, the concentration of $LaCl_3$ was assumed from the measured weights of chlorides added to the crucibles. The intervals for D_o were determined with 95% confidence by assuming a student's t-distribution for each CV test.

Table 2
Diffusion Coefficients for $LaCl_3$ in $CaCl_2$-LiCl with varying concentration and temperature.

Test	Temp (°C)	ICP-MS Evaluation	wt% LaCl3	D_o (10^{-5} cm^2 s^{-1})	
				Best Fit	± 95% CI
CV1	697.8	No	1	1.92	0.0742
CV2	802.7	No	1	2.37	0.0994
CV3	820.8	Yes	2.2	1.67	0.0108
CV4	822.0	Yes	1.5	1.86	0.0749

According to Table 2, D_o for $LaCl_3$ in $CaCl_2$-LiCl is within the same order of magnitude and is greater than other values for similar salt systems at lower temperatures in the literature. For example, D_o was found to be 0.176×10^{-5} cm^2 s^{-1} for 3 wt% $LaCl_3$ in eutectic LiCl-KCl at 500°C [45], 0.289×10^{-5} cm^2 s^{-1} at 550°C [32], and 0.831×10^{-5} cm^2 s^{-1} at 525°C and 2 wt% $LaCl_3$ [45]. Also, D_o was found to be 1.17×10^{-5} cm^2 s^{-1} for 7×10^{-5} mol cm^{-3} $LaCl_3$ in eutectic LiCl-KCl at 450°C [22]. D_o was found to be 0.97×10^{-5}cm^2 s^{-1} for 1.7×10^{-4} mol cm^{-3} $LaCl_3$ in equimolar $CaCl_2$-NaCl at 550°C [22]. Due to the uncertainty in the concentration of $LaCl_3$ in CV1 and CV2, a trend cannot be verified. Despite the uncertainty, some of the data supports the expected behavior for this salt system. For example, D_o increases with temperature between CV1 and CV2.

Data at higher scan rates (>1.5 V s^{-1}) in CV4 was omitted from determining D_o. The La reduction peak height showed oscillation and a slight upward curvature from linearity (see Figure 6). This curvature may result from surface area growth as higher current densities occurred, leading to La dendrites [21,67]. Due to this behavior, such reduction peak heights were excluded from D_o calculations.

3.1.5. Standard Apparent Potential

The standard apparent potential was determined for $LaCl_3$ in $CaCl_2$-LiCl using the following Berzins-Delahay equation [50] (for soluble-insoluble systems):

$$E_p = E^{o\prime} + \frac{RT}{nF}\ln x_o - 0.854\frac{RT}{nF} \tag{11}$$

E_p is the potential (V), $E^{o'}$ is the standard apparent potential (V), n is the number of electrons exchanged, x_o is the molar concentration of analyte, and T is the temperature of the salt (K). Because the composition of the RE varied between experimental sets, the standard apparent potentials were all adjusted to a 5 mol% AgCl RE composition by the following relation:

$$E_{p-exp} - E_{p-5mol\%} = \frac{RT}{nF}\ln\frac{x_{o-exp}}{x_{o-5mol\%}} \tag{12}$$

$x_{o\text{-}exp}$, $x_{o\text{-}5mol\%}$, $E_{p\text{-}exp}$, and $E_{p\text{-}5mol\%}$ (V), are the AgCl molar concentrations and the peak potentials of the experimental and 5 mol% AgCl REs respectively. The calculated and standardized (i.e., adjusted to 5 mol% AgCl) standard apparent potentials are given in Table 3. The intervals for $E^{o'}$ were determined with 95% confidence by assuming a student's t-distribution for each CV test.

Table 3
The standard apparent potential for La^{3+}/La couple in $CaCl_2$-LiCl.

Test	E_o' (V)		
	Average Potential	Adjusted Potential	+/- 95% CI

https://doi.org/10.1016/j.jelechem.2022.116442

CV1	-2.178	-2.180	0.006
CV2	-2.026	-2.028	0.003
CV3	-1.809	-1.810	0.001
CV4	-1.881	-1.880	0.003

3.2. $LaCl_3$ in $CaCl_2$

A 'window' CV for $LaCl_3$ in $CaCl_2$ is shown in Figure 11. In this and the CVs that follow for this salt mixture, La is suspected to reduce and electrodeposit prior to Ca. As the potential increases following reduction, Ca is suspected to oxidize prior to La. At approximately 0.4V, the current density increases slightly. This is suspected to be the electrode (in this case, W) oxidizing due to residual oxygen ions in the melt [68]. Note that the La reduction peak is difficult to distinguish from the Ca reduction peak.

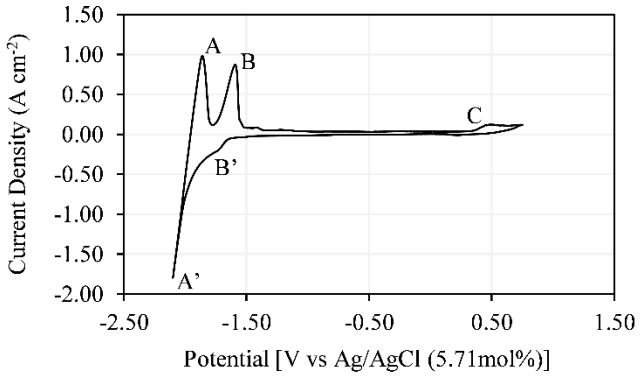

Figure 11. Cyclic voltammogram from test CV5 at 200 mV s^{-1}. A/A': Ca oxidation/reduction; B/B': La oxidation/reduction; C: W oxidation.

For this salt system, the La reduction peak height and potential were also evaluated from the baseline as a function of scan rate to determine electrochemical behavior. It was suspected that the baseline of the La reduction peak decreased or 'curved' in current density as the applied potential decreased. The CVs of pure $CaCl_2$ were recorded and compared with $LaCl_3$ in $CaCl_2$ (see Figure 12) to verify if the reduction peak baseline was relatively flat compared to the decrease in current density representing the reduction of La (as was observed for the $CaCl_2$-LiCl salt system). Evaluating the $CaCl_2$ baseline faced some challenges. In Figure 12, the baseline for the gray curve remains relatively flat leading up to B', rather than gradually rising like the black curve. Unlike the CV overlay of $CaCl_2$-LiCl and $LaCl_3$ in $CaCl_2$-LiCl, the Ca reduction peak in the $CaCl_2$ baseline overlaps the La reduction peak. This occurred twice in different electrolytic cells notwithstanding minimal temperature differences (<5°C) and using the same RE. There is a notable shift in electrochemical behavior with La ions present. The change in behavior casts uncertainty on a simple background subtraction approach. Because of the overlap and shift in behavior, it was not possible to accurately determine the baseline trend.

https://doi.org/10.1016/j.jelechem.2022.116442

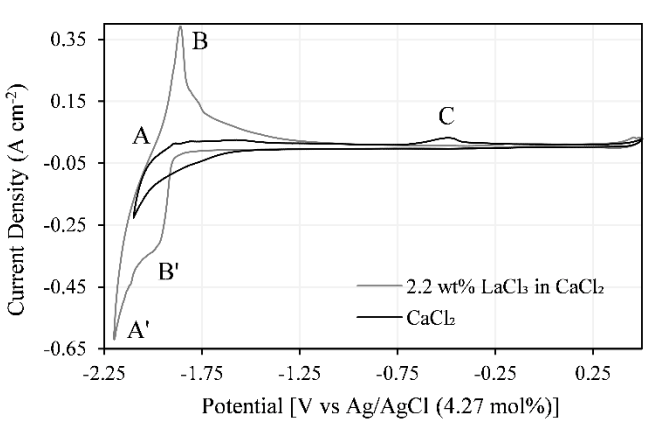

Figure 12. CV for CV6 test at 200 mV s^{-1} overlaid on pure $CaCl_2$ at 200 mV s^{-1} with no resistance compensation (WE: 1.5mm W rod with area of approximately 0.56 cm^2, at temperatures 822°C, CE: 3mm W rod, RE: same RE used for CV6). A/A': Ca oxidation/reduction; B/B': La oxidation/reduction; C: Contaminant oxidation.

3.2.1. Scan Rate Relationships

The current rises with scan rate in Figure 13, but there were challenges in quantifying the peak heights and potentials. Distinguishing the La reduction peaks from the Ca reduction peaks was difficult, partially due to the proximity of the La and Ca reduction peak potentials. The La reduction peaks are even more difficult to distinguish in $CaCl_2$ than in $CaCl_2$-LiCl. This challenge extended up to high scan rates (2.5 V s^{-1}). Consequently, using direct measurements from the software accompanying the potentiostat to estimate the peak heights and positions are not reliable.

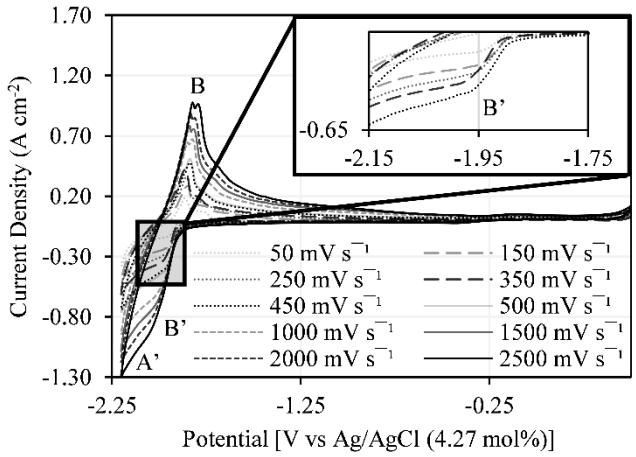

Figure 13. Overlay of cyclic voltammograms at select scan rates for test CV6. A': Ca reduction; B/B': La oxidation/reduction.

The La reduction peak heights and positions were determined by semi-differential (SD) analysis [69–72,17]. The SD CV profile is compared to the directly measured CV profile in Figure 14. Although the reduction peaks are difficult to distinguish via direct measurements, the peaks are much more obvious after semi-differentiation (see Figure 14).

 https://doi.org/10.1016/j.jelechem.2022.116442

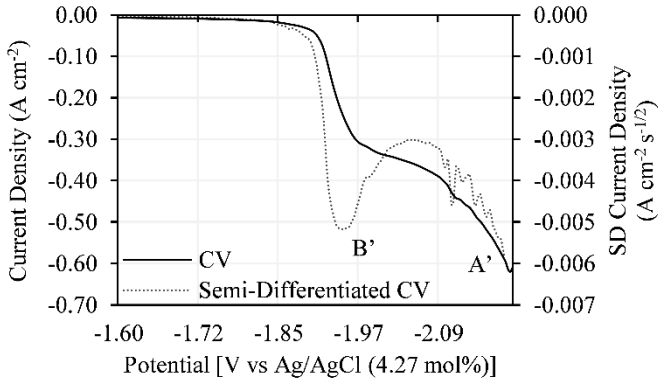

Figure 14. Overlay of CV and Semi-differentiated CV of CV6 at 200 mV s^{-1}. A': Ca reduction; B': La reduction.

In SD analysis of CVs, there seems to be a relationship between the reduction peak heights and positions with scan rate. The SD peak current appears linear with scan rate for reversible and irreversible reactions (see Figure 15). The SD peak current has a trend that deviates from linearity with respect to scan rate and the reduction peak position is not independent of scan rate (see Figures 15 and 16). In the CV6 test, the reduction peak heights deviated from linearity at approximately the same scan rate (300 mV s^{-1}) in which the peak position deviated from scan rate independence (see Figure 16). These relationships for the SD data, and the consistent point in deviation (in the case of CV6) indicate that there may be a transition from electrochemical reversibility to irreversibility for $LaCl_3$ in $CaCl_2$.

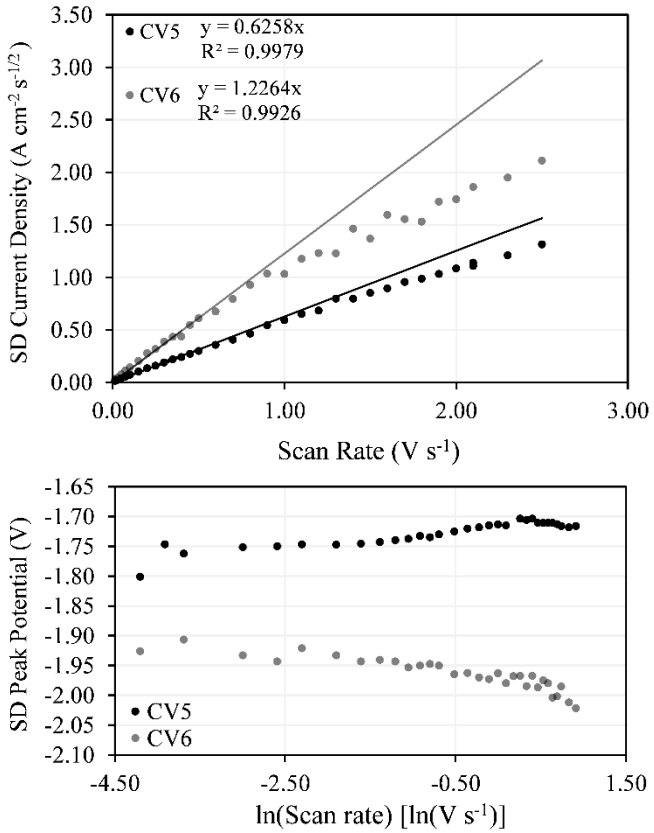

Figure 15. Plots of semi-differentiated peak height versus square root of scan rate (top) and peak position versus natural logarithm of scan rate for all tests in $CaCl_2$.

https://doi.org/10.1016/j.jelechem.2022.116442

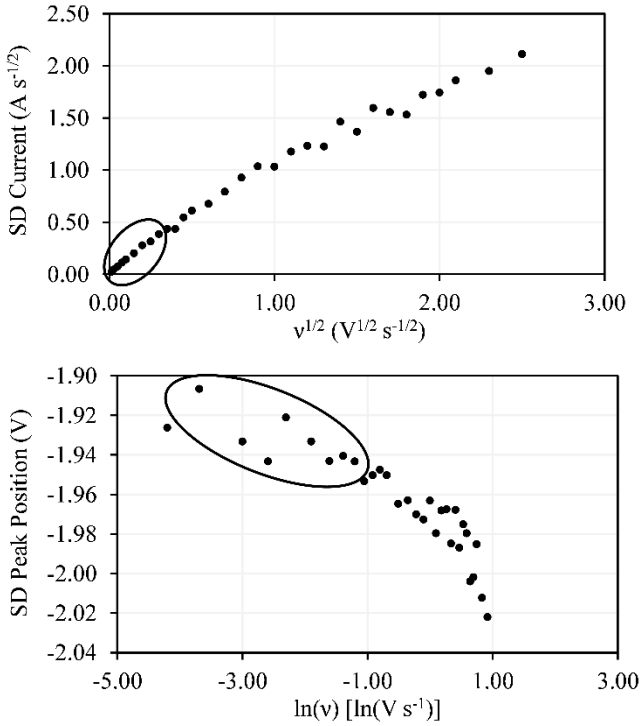

Figure 16. Semi-differentiated peak height versus square root of scan rate (top) and peak position versus natural logarithm of scan rate (bottom) for test CV6.

However, the CV5 test differs from the CV6 test. In the CV5 test, the peak potential departs from scan rate independence in the opposite direction, then stabilizes. It is unusual that the trends in peak position with scan rate show different trends between experiments. The peak potentials between the CV5 and CV6 data sets (see Figure 16) differ significantly due to differences in the temperatures and mol% of AgCl in the REs.

The inconsistent results between CV5 and CV6 highlight the difficulty in analyzing metal deposition peaks with significant interference and the need to improve the theoretical underpinning and data handling of semi-differentiated metal reduction peaks. For example, the difference in trends of peak height and potential may be an artifact of the data or due to differences in the extent of area growth and dendrite formation. Regarding data artifacts, it is observed that, as the scan rate increases, the noise in the SD data increases. This is due to the current being sampled at fixed potential steps. As the scan rate increases, the peak rises more sharply, resulting in a greater difference in current between data points. When the discrete data points are semi-differentiated, this difference becomes even more pronounced, leading to greater uncertainty in where the true peak potential and current lies between data points. The CV step potential was consistent through all experiments (software default -2.44 mV). Evaluating the effects of varying the CV step potential may elucidate the relationship between the resolution of SD data and peak currents and potentials, yielding insight into the potential error introduced due to semi-differentiation. Further investigation into the proper techniques and development of theory to support the interpretation of the SD metal deposition peaks would yield a valuable tool in electroanalysis of complex systems.

3.2.2. Diffusion Coefficients

To determine diffusion coefficients from semi-differentiated peak height (e_p), Eq. (13) was suggested in literature for soluble-insoluble reactions [72]:

$$e_p = \frac{n^2 F^2 A C \sqrt{D_o}}{2RT} \tag{13}$$

 https://doi.org/10.1016/j.jelechem.2022.116442

Eq. (13) was modified to Eq. (14) by substituting in E_o-vt for E(t) in the derivation presented by Tylka et al.[72] as was done in the case of soluble-soluble reactions [70]:

$$e_p = \frac{n^2F^2AC\sqrt{D_o}}{2RT}\nu \tag{14}$$

Using Eq. (14), D_o was calculated for $LaCl_3$ in $CaCl_2$ (see Table 4). The derived D_o is somewhat comparable with that found in literature derived via SD techniques. For example, D_o was found to be 1.04×10^{-5} cm^2 s^{-1} for 0.96 wt% $LaCl_3$ in eutectic LiCl-KCl at 500°C [45] and 1.15×10^{-5} cm^2 s^{-1} with $7x10^{-5}$ mol cm^{-3} $LaCl_3$ at 450°C [22]. D_o was found to be 0.95×10^{-5} cm^2 s^{-1} for 1.7×10^{-4} mol cm^{-3} $LaCl_3$ in equimolar $CaCl_2$-NaCl at 550°C [22]. It was assumed that $CaCl_2$ and $LaCl_3$ formed an ideal mixture, with additive volumes. The volumes of $CaCl_2$ and $LaCl_3$ were determined from empirical relations [65,66]. ICP-MS was conducted for experiment CV6 to verify the concentration of $LaCl_3$ in the molten salts—this concentration was used to determine D_o. However, a salt sample was not available from CV5 for chemical analysis. In this case, the concentration of $LaCl_3$ was assumed from the measured weights of chlorides added to the crucibles. D_o was estimated by assuming that the baseline was 'flat' relative to the decrease in SD current density representing the reduction to La. Although the derived D_o compares to that found in literature, the validity of using Eq. (8) and assuming a 'flat' baseline for semi-differentiated CV data require verification through additional theoretical development and experimentation.

Table 4
Diffusion Coefficients for $LaCl_3$ in $CaCl_2$ with varying concentration and temperature.

Test	Temp (°C)	ICP-MS Evaluation	wt% LaCl3	D_o (10^{-5} cm^2 s^{-1})	
				Best Fit	± 95% CI
CV5	794.5	No	2	0.264	0.000565
CV6	823.1	Yes	2.2	0.989	0.0195

3.2.3. Standard Apparent Potential

The standard apparent potential for La^{3+} reduction to La was calculated using Eq. (15) [72]:

$$E_p = E^{o\prime} + \frac{RT}{nF}\ln\frac{x_o}{2} \tag{15}$$

E_p in this case is the potential (V) for SD data. The value of the standard apparent potential was adjusted to a 5 mol% AgCl RE potential for comparative purposes like what was done in Eq. (12). The resulting values for the standard apparent potential for La^{3+}/La couple are given in Table 5.

Table 5
The standard apparent potential for La^{3+}/La couple in $CaCl_2$.

Test	E_o' (V)		
	Average Potential	Adjusted Potential	+/- 95% CI
CV5	-1.557	-1.561	0.006
CV6	-1.789	-1.784	0.008

3.3. Electroanalytical Methods

The electroanalytical measurements required improved experimental techniques to perform appropriate measurements. Improvements included housing the electrolytic cell in a grounded faraday cage and using electrode

 https://doi.org/10.1016/j.jelechem.2022.116442

rods as opposed to wires. Various sizes and types of ceramic, salt, and electrode wire were compared to optimize RE performance. Other improvements included electrode positioning in the electrolytic cell. The grounded faraday cage protected the electrolytic cell and electrodes from electromagnetic radiation from the furnace heating coils. Transitioning from coiled wire to larger rods for the CE eliminated shorting. Thinned mullite and alumina tubes (1-2mm walls), and thin Ag wire (~0.5mm OD) resulted in a stable reference potential. Alumina tubes that did not require thinning resulted in easier construction and elimination of structurally weak points due to stresses introduced while machining the tube thinner. Additional changes minimized oxide contamination and improved electrode cleaning. Observations indicated the importance of choosing a correct resistance compensation applied to the electrolytic cell.

3.3.1. Oxides and Electrodes

For some experiments, CVs visibly indicated oxide contamination of the analyte. This occurred when $CaCl_2$ and $CaCl_2$-LiCl were not pre-melted prior to the addition of the analyte. To minimize oxide and moisture contamination, chlorides were melted for ≥30 minutes and cooled, at least once, prior to adding and performing electrochemical analysis on $LaCl_3$.

In addition, for CV6, some contaminant was reduced prior to La reduction (see Figure 17). A possible explanation for this reduction is the electrode was not properly 'cleaned' prior to experimentation. In subsequent scans, the potential was increased high enough (up to 0.5V) to oxidize the WE more fully—stripping or 'cleaning' the contaminant from the electrode—while avoiding electrode oxidation. Driving the potential more positive for subsequent scans led to decreases in the current density of C' until it was negligible.

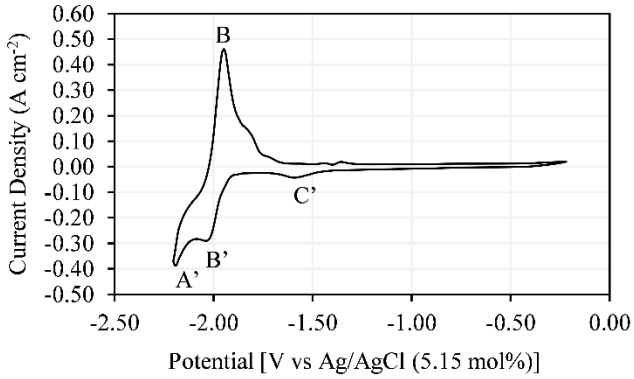

Figure 17. CV of CV6 at 100 mV s^{-1} prior to anodic cleaning of WE. A': Ca reduction; B/B': La oxidation/reduction; C': Contaminant reduction.

3.3.2. Resistance Compensation

The applied resistance compensation was varied between scans. The varying compensated resistances—differing by even 0.1Ω—led to differing current densities (see Figure 18). Knowing the appropriate resistance compensation to apply to molten salts, while avoiding under- or overcompensation, is vital despite the low resistance due to high currents.

https://doi.org/10.1016/j.jelechem.2022.116442

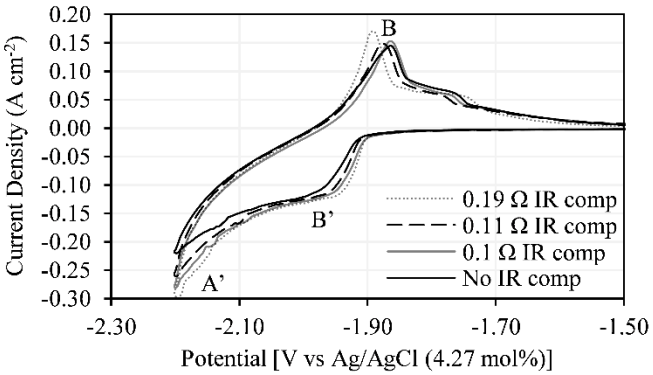

Figure 18. CV6 at 100 mV s^{-1} with varying resistance compensation. A': Ca reduction; B/B': La oxidation/reduction.

4. Conclusions

For $LaCl_3$ in $CaCl_2$-LiCl, La reduction peak heights were calculated assuming a 'flat' baseline compared to the decrease in current density with respect to potential representing La reduction. La reduction peak heights and Berzins-Delahay relations were used to estimate values of D_o, which were consistent with values from similar salt systems. The dependence of La reduction peak height and the independence of La reduction peak position on scan rate indicate that the salt system is reversible up to scan rates as high as 2.5 V s^{-1}. La reduction peak potentials at low scan rates (<100 mV s^{-1}) could not be accurately distinguished from Ca reduction. The Berzins-Delahay relations underestimated the number of electrons exchanged, *n*. A complete comparison of the theoretically calculated Berzins-Delahay peak profile to the experimentally measured peak profile revealed the experimental peak to be broader, which is suggested to be due to the deposition onto a foreign substrate (i.e., non-unity activity of the deposited metal). Improving models for predicting electrodeposition of this and similar salt systems is needed for more accurate and consistent results. Nonetheless, more accurate values of *n* (2.98 and 2.93) were calculated via SWV and models for metal deposition onto a foreign substrate.

For $LaCl_3$ in $CaCl_2$, the reduction peak heights and positions could not confidently be determined using direct measurements due to significant overlap of La reduction peaks and Ca reduction. SD data clearly distinguished La reduction peaks from Ca reduction. However, the dependence of SD data on scan rate is not clear. Further refinement of semi-differentiation of discrete metal deposition peak data is needed to ensure that artifacts are not introduced in the analysis. Nonetheless, SD analysis provided a path forward to analyze the La deposition peak and enable the calculation of properties within the range of scan rates where reversibility could confidently be assumed.

Electroanalytical practices developed throughout experimentation. Housing the electrolytic cell in a grounded, faraday cage shielded the experiments from electromagnetic radiation. Using rods rather than wires enhanced electrode consistency and minimized electric shorts. Positioning the electrodes away from the furnace's heating coils also minimized electrical interference. Pre-melting and cooling salts prior to experimentation minimized moisture content. Electrode contamination was minimized by driving the potential to just before the electrode's oxidation point. Also, varying resistance compensation demonstrated the variance of current response at the electrode. Even 'slight' differences in compensation risk under- or overcompensation. The effects of varying resistance compensation on reaction values determined via Berzins-Delahay relations and semi-differential relations also requires additional investigation.

5. Acknowledgements

This work was performed under the auspices of the U.S. Department of Energy by Lawrence Livermore National Laboratory under Contract DE-AC52-07NA27344. Data analysis and visualization was aided by Daniel's XL Toolbox add-in for Excel, version 7.3.2, by Daniel Kraus, Würzburg, Germany (www.xltoolbox.net).

 https://doi.org/10.1016/j.jelechem.2022.116442

6. References

[1] U.S. Department of the Interior, Final List of Critical Minerals 2018, Fed. Regist. 83 (2018) 23295–23296.

[2] European Commission, Study on the review of the list of critical raw materials : critical raw materials factsheets., Publ. Off. Eur. Union. (2017). http://op.europa.eu/en/publication-detail/-/publication/7345e3e8-98fc-11e7-b92d-01aa75ed71a1 (accessed March 24, 2021).

[3] S.M. Hayes, E.A. McCullough, Critical minerals: A review of elemental trends in comprehensive criticality studies, Resour. Policy. 59 (2018) 192–199. https://doi.org/10.1016/j.resourpol.2018.06.015.

[4] G. Charalampides, K.I. Vatalis, B. Apostoplos, B. Ploutarch-Nikolas, Rare Earth Elements: Industrial Applications and Economic Dependency of Europe, Procedia Econ. Finance. 24 (2015) 126–135. https://doi.org/10.1016/S2212-5671(15)00630-9.

[5] Rare earth recovery and automotive growth, Roskill Wood Mackenzie Bus. (2017). https://roskill.com/news/rare-earth-recovery-automotive-growth/ (accessed July 28, 2021).

[6] W.D. Judge, G. Azimi, Recent progress in impurity removal during rare earth element processing: A review, Hydrometallurgy. 196 (2020) 105435. https://doi.org/10.1016/j.hydromet.2020.105435.

[7] L. Wang, X. Huang, Y. Yu, L. Zhao, C. Wang, Z. Feng, D. Cui, Z. Long, Towards cleaner production of rare earth elements from bastnaesite in China, J. Clean. Prod. 165 (2017) 231–242. https://doi.org/10.1016/j.jclepro.2017.07.107.

[8] Y. Sakamura, T. Hijikata, K. Kinoshita, T. Inoue, T.S. Storvick, C.L. Krueger, L.F. Grantham, S.P. Fusselman, D.L. Grimmett, J.J. Roy, Separation of Actinides from Rare Earth Elements by Electrorefining in LiC1-KC1 Eutectic Salt, J. Nucl. Sci. Technol. 35 (1998) 49–59. https://doi.org/10.1080/18811248.1998.9733819.

[9] M. Bertolus, M. Defranceschi, Toward the Comparison of Rare Earth Element and Actinide Behavior in Materials: A Computational Study of Ce- and U-Bearing Britholites, J. Phys. Chem. B. 110 (2006) 19226–19232. https://doi.org/10.1021/jp0629083.

[10] F.R. Hartley, The preparation of anhydrous lanthanon chlorides by high-temperature chlorination of monazite, J. Appl. Chem. 2 (1952) 24–31. https://doi.org/10.1002/jctb.5010020107.

[11] P. Okabe, M. Newton, D. Rappleye, M.F. Simpson, Gas-solid reaction pathway for chlorination of rare earth and actinide metals using hydrogen and chlorine gas, J. Nucl. Mater. 534 (2020) 152156. https://doi.org/10.1016/j.jnucmat.2020.152156.

[12] P. Okabe, D. Rappleye, M. Newton, M.F. Simpson, Development of metallic nuclear material purification process via simultaneous chlorination and volatilization, J. Nucl. Mater. 543 (2021) 152626. https://doi.org/10.1016/j.jnucmat.2020.152626.

[13] F.H. Spedding, A.H. Daane, The Preparation of Rare Earth Metals, J. Am. Chem. Soc. 74 (1952) 2783–2785. https://doi.org/10.1021/ja01131a024.

[14] C.K. Gupta, N. Krishnamurthy, Extractive metallurgy of rare earths, Int. Mater. Rev. 37 (1992) 197–248. https://doi.org/10.1179/imr.1992.37.1.197.

[15] N. KRISHNAMURTHY, C.K. GUPTA, Rare Earth Metals and Alloys by Electrolytic Methods, Miner. Process. Extr. Metall. Rev. 22 (2001) 477–507. https://doi.org/10.1080/08827509808962512.

[16] F. Lantelme, Y. Berghoute, Electrochemical Studies of LaCl3 and GdCl3 Dissolved in Fused LiCl-KCl, J. Electrochem. Soc. 146 (1999) 4137–4144. https://doi.org/10.1149/1.1392604.

[17] D. Rappleye, M.L. Newton, C. Zhang, M.F. Simpson, Electroanalytical measurements of binary-analyte mixtures in molten LiCl-KCl eutectic: Uranium(III)- and Magnesium(II)-Chloride, J. Nucl. Mater. 486 (2017) 369–380. https://doi.org/10.1016/j.jnucmat.2017.01.047.

[18] P. Bagri, M.F. Simpson, Determination of activity coefficient of lanthanum chloride in molten LiCl-KCl eutectic salt as a function of cesium chloride and lanthanum chloride concentrations using electromotive force measurements, J. Nucl. Mater. 482 (2016) 248–256. https://doi.org/10.1016/j.jnucmat.2016.10.006.

[19] S. Guo, E. Wu, J. Zhang, Investigation of electrochemical kinetics for La(III)/La reaction in molten LiClKCl eutectic salt using potentiometric polarization, J. Nucl. Mater. 510 (2018) 414–420. https://doi.org/10.1016/j.jnucmat.2018.08.036.

[20] S.P. Fusselman, J.J. Roy, D.L. Grimmett, L.F. Grantham, C.L. Krueger, C.R. Nabelek, T.S. Storvick, T. Inoue, T. Hijikata, K. Kinoshita, Y. Sakamura, K. Uozumi, T. Kawai, N. Takahashi, Thermodynamic Properties for Rare Earths and Americium in Pyropartitioning Process Solvents, J. Electrochem. Soc. 146 (1999) 2573. https://doi.org/10.1149/1.1391974.

[21] H. Tang, B. Pesic, Electrochemical behavior of LaCl3 and morphology of La deposit on molybdenum substrate in molten LiCl–KCl eutectic salt, Electrochimica Acta. 119 (2014) 120–130. https://doi.org/10.1016/j.electacta.2013.11.148.
[22] Y. Castrillejo, M.R. Bermejo, A.M. Martínez, A.P. Díaz, Electrochemical behavior of lanthanum and yttrium ions in two molten chlorides with different oxoacidic properties: The eutectic LiCl-KCl and the equimolar mixture CaCl2-NaCl, J. Min. Metall. Sect. B Metall. 39 (2003) 109–135.
[23] P. Masset, R.J.M. Konings, R. Malmbeck, J. Serp, J.-P. Glatz, Thermochemical properties of lanthanides (Ln=La,Nd) and actinides (An=U,Np,Pu,Am) in the molten LiCl–KCl eutectic, J. Nucl. Mater. 344 (2005) 173–179. https://doi.org/10.1016/j.jnucmat.2005.04.038.
[24] C.P. Fabian, V. Luca, P. Chamelot, L. Massot, C. Caravaca, G.R. Lumpkin, Experimental and Simulation Study of the Electrode Reaction Mechanism of La3+ in LiCl-KCl Eutectic Molten Salt, J. Electrochem. Soc. 159 (2012) F63. https://doi.org/10.1149/2.057204jes.
[25] A. Samin, Z. Wang, E. Lahti, M. Simpson, J. Zhang, Estimation of key physical properties for LaCl3 in molten eutectic LiCl–KCl by fitting cyclic voltammetry data to a BET-based electrode reaction kinetics model, J. Nucl. Mater. 475 (2016) 149–155. https://doi.org/10.1016/j.jnucmat.2016.04.002.
[26] W. Han, W. Wang, M. Li, D. Wang, H. Li, J. Chen, Y. Sun, Electrochemical separation of La from LiCl-KCl fused salt by forming La-Pb alloys, Sep. Purif. Technol. 275 (2021) 119188. https://doi.org/10.1016/j.seppur.2021.119188.
[27] Y. Castrillejo, M.R. Bermejo, E. Barrado, A.M. Martínez, P. Díaz Arocas, Solubilization of rare earth oxides in the eutectic LiCl–KCl mixture at 450°C and in the equimolar CaCl2–NaCl melt at 550°C, J. Electroanal. Chem. 545 (2003) 141–157. https://doi.org/10.1016/S0022-0728(03)00092-5.
[28] C.K. Gupta, N. Krishnamurthy, Oxide reduction processes in the preparation of rare-earth metals, Min. Metall. Explor. 30 (2013) 38–44. https://doi.org/10.1007/BF03402339.
[29] D.K. Sahoo, H. Singh, N. Krishnamurthy, Current efficiency in electro-winning of lanthanum and cerium metals from molten chloride electrolytes, Rare Met. 32 (2013) 305–311. https://doi.org/10.1007/s12598-013-0060-y.
[30] V.P. Kochergin, R.N. Obozhina, T.I. Dragoshanskaya, B.P. Startsev, High-temperature corrosion of lanthanum in equimole mixture of sodium and potassium chlorides, Zashchita Met. 20 (1984) 310–312.
[31] A.L. Glagolevskaya, S.A. Kuznetsov, E.G. Polyakov, P.T. Stangrit, Electrochemical reduction of lanthanum trichloride in the melt of sodium and potassium chlorides of equimolar composition, Zhurnal Prikl. Khimii. 60 (1987) 770–774.
[32] J. Zhang, S. Guo, Rare Earth Electrochemical Property Measurements and Phase Diagram Development in a Complex Molten Salt Mixture for Molten Salt Recycle, 2018. https://doi.org/10.2172/1432448.
[33] P.J. Masset, Thermogravimetric study of the dehydration reaction of LiCl·H2O, J. Therm. Anal. Calorim. 96 (2009) 439–441. https://doi.org/10.1007/s10973-008-9399-y.
[34] M. Molenda, J. Stengler, M. Linder, A. Wörner, Reversible hydration behavior of CaCl2 at high H2O partial pressures for thermochemical energy storage, Thermochim. Acta. 560 (2013) 76–81. https://doi.org/10.1016/j.tca.2013.03.020.
[35] D.K. Sahoo, R. Mishra, H. Singh, N. Krishnamurthy, Determination of thermodynamic stability of lanthanum chloride hydrates (LaCl3·xH2O) by dynamic transpiration method, J. Alloys Compd. 588 (2014) 578–584. https://doi.org/10.1016/j.jallcom.2013.11.115.
[36] K. Yasuda, T. Nohira, Y.H. Ogata, Y. Ito, Electrochemical window of molten LiCl–KCl–CaCl2 and the Ag+/Ag reference electrode, Electrochimica Acta. 51 (2005) 561–565. https://doi.org/10.1016/j.electacta.2005.05.014.
[37] D. Sri Maha Vishnu, N. Sanil, K.S. Mohandas, K. Nagarajan, Electrochemical characterisation of CaCl2 deficient LiCl–KCl–CaCl2 eutectic melt and electro-deoxidation of solid UO2, J. Nucl. Mater. 470 (2016) 179–186. https://doi.org/10.1016/j.jnucmat.2015.12.003.
[38] W. Zhang, C.R. Pulham, A.R. Mount, N. Brockie, R. Lewin, Thermodynamic calculation and reference electrode calibration for high temperature molten salts, Energy Mater. 3 (2008) 132–136. https://doi.org/10.1179/174892408X394254.
[39] I. Barin, Thermochemical Data of Pure Substances, 3rd ed., VCH Verlagsgesellschaft mbH., Weinheim, 1995.
[40] K.A. Gschneidner, F.W. Calderwood, Ca−La (Calcium-Lanthanum) Phase Diagram, in: P. Villars, H. Okamoto, K. Cenzual (Eds.), ASM Alloy Phase Diagr. Database, ASM International, Materials Park, OH, 2016: pp. 515–516. https://doi.org/10.1007/BF02879421 (accessed April 15, 2022).

[41] H. Okamoto, La−Li (Lanthanum-Lithium) Phase Diagram, in: P. Villars, H. Okamoto, K. Cenzual (Eds.), ASM Alloy Phase Diagr. Database, ASM International, Materials Park, OH, 2016: pp. 515–516. https://doi.org/10.1007/BF02879421 (accessed April 15, 2022).
[42] S. Natsui, T. Sudo, T. Kaneko, K. Tonya, D. Nakajima, T. Kikuchi, R.O. Suzuki, Spontaneous colloidal metal network formation driven by molten salt electrolysis, Sci. Rep. 8 (2018) 13114. https://doi.org/10.1038/s41598-018-31521-3.
[43] A.B. Ivanov, V.A. Volkovich, D.A. Poskryakov, B.D. Vasin, T.R. Griffiths, Electrode potentials of tungsten in fused alkali chlorides, AIP Conf. Proc. 1767 (2016) 020010. https://doi.org/10.1063/1.4962594.
[44] M.W. Chase, JANAF Thermochemical Tables, NIST Standard Reference Database 13, NIST-JANAF Thermochem. Tables. (1986). https://doi.org/10.18434/T42S31.
[45] M.F. Simpson, S. Phongikaroon, J. Zhang, Development and Optimization of Voltammetric Methods for Real Time Analysis of Electrorefiner Salt with High Concentrations of Actinides and Fission Products, 2018. https://doi.org/10.2172/1432793.
[46] B. Prabhakara Reddy, S. Vandarkuzhali, T. Subramanian, P. Venkatesh, Electrochemical studies on the redox mechanism of uranium chloride in molten LiCl–KCl eutectic, Electrochimica Acta. 49 (2004) 2471–2478. https://doi.org/10.1016/j.electacta.2004.02.002.
[47] P. Masset, D. Bottomley, R. Konings, R. Malmbeck, A. Rodrigues, J. Serp, J.-P. Glatz, Electrochemistry of Uranium in Molten LiCl-KCl Eutectic, J. Electrochem. Soc. 152 (2005) A1109. https://doi.org/10.1149/1.1901083.
[48] S.A. Kuznetsov, H. Hayashi, K. Minato, M. Gaune-Escard, Electrochemical Behavior and Some Thermodynamic Properties of UCl[sub 4] and UCl[sub 3] Dissolved in a LiCl-KCl Eutectic Melt, J. Electrochem. Soc. 152 (2005) C203. https://doi.org/10.1149/1.1864532.
[49] K.C. Marsden, B. Pesic, Evaluation of the Electrochemical Behavior of CeCl3 in Molten LiCl-KCl Eutectic Utilizing Metallic Ce as an Anode, J. Electrochem. Soc. 158 (2011) F111. https://doi.org/10.1149/1.3575637.
[50] T. Berzins, P. Delahay, Oscillographic Polarographic Waves for the Reversible Deposition of Metals on Solid Electrodes, J. Am. Chem. Soc. 75 (1953) 555–559. https://doi.org/10.1021/ja01099a013.
[51] A. Szabo, D.K. Cope, D.E. Tallman, P.M. Kovach, R.M. Wightman, Chronoamperometric current at hemicylinder and band microelectrodes: Theory and experiment, J. Electroanal. Chem. Interfacial Electrochem. 217 (1987) 417–423. https://doi.org/10.1016/0022-0728(87)80233-4.
[52] A.J. Bard, L.R. Faulkner, Electrochemical methods: fundamentals and applications, 2nd ed, Wiley, New York, 2001.
[53] T. Williams, R. Shum, D. Rappleye, Concentration Measurements In Molten Chloride Salts Using Electrochemical Methods, J. Electrochem. Soc. 168 (2021) 123510. https://doi.org/10.1149/1945-7111/ac436a.
[54] D. Yoon, Electrochemical Studies of Cerium and Uranium in LiCl-KCl Eutectic for Fundamentals of Pyroprocessing Technology, VCU Libraries, 2016. https://doi.org/10.25772/KKEK-QN30.
[55] G.-Z. Wang, Y. Liu, D.-B. Ji, L.-Y. Zhu, D.-Q. Ji, D. Yuan, M.-L. Zhang, H.-J. Wu, Electrochemical preparation and properties of a Mg–Li–Y alloy *via* co-reduction of Mg(II) and Y(III) in chloride melts, RSC Adv. 11 (2021) 13839–13847. https://doi.org/10.1039/D1RA01349A.
[56] A. Samin, E. Wu, J. Zhang, The thermodynamic and transport properties of GdCl3 in molten eutectic LiCl-KCl derived from the analysis of cyclic voltammetry signals, J. Appl. Phys. 121 (2017) 074904. https://doi.org/10.1063/1.4976570.
[57] A. Osipenko, A. Mayershin, V. Smolenski, A. Novoselova, M. Kormilitsy, Electrochemistry of Curium in Molten Chlorides, in: U.K. Sur (Ed.), Recent Trend Electrochem. Sci. Technol., InTech, 2012. https://doi.org/10.5772/38935.
[58] N. Fatouros, D. Krulic, H. Groult, Linear sweep and staircase voltammetries for reversible deposition of metal ions on the same metal and on foreign substrates, J. Electroanal. Chem. 625 (2009) 1–6. https://doi.org/10.1016/j.jelechem.2008.07.028.
[59] N. Fatouros, D. Krulic, Analysis of the square wave voltammetry for reversible metal deposition on a foreign substrate – Experimental study of silver deposition on gold, J. Electroanal. Chem. 706 (2013) 76–85. https://doi.org/10.1016/j.jelechem.2013.07.019.
[60] R. Fuller, T. Williams, M. Schvaneveldt, D. Rappleye, A comparison of square-wave voltammetry models to determine the number of electrons exchanged in metal deposition, Electrochimica Acta. 414 (2022) 140220. https://doi.org/10.1016/j.electacta.2022.140220.
[61] G.C. Barker, I.L. Jenkins, Square-wave polarography, Analyst. 77 (1952) 685–696. https://doi.org/10.1039/AN9527700685.

[62] L. Ramaley, M.S. Krause, Theory of square wave voltammetry, Anal. Chem. 41 (1969) 1362–1365. https://doi.org/10.1021/ac60280a005.
[63] K. Aoki, K. Tokuda, H. Matsuda, J. Osteryoung, Reversible square-wave voltammograms independence of electrode geometry, J. Electroanal. Chem. Interfacial Electrochem. 207 (1986) 25–39. https://doi.org/10.1016/0022-0728(86)87060-7.
[64] G.J. Janz, R.P.T. Tomkins, C.B. Allen, J.R. Downey, G.L. Garner, U. Krebs, S.K. Singer, Molten salts: Volume 4, part 2, chlorides and mixtures—electrical conductance, density, viscosity, and surface tension data, J. Phys. Chem. Ref. Data. 4 (1975) 871–1178. https://doi.org/10.1063/1.555527.
[65] G.J. Janz, Thermodynamic and transport properties for molten salts: correlation equations for critically evaluated density, surface tension, electrical conductance, and viscosity data, American Institute of Physics, New York, NY, 1988.
[66] P.M. Nasch, S.G. Steinemann, Density and Thermal Expansion of Molten Manganese, Iron, Nickel, Copper, Aluminum and Tin by Means of the Gamma-Ray Attenuation Technique, Phys. Chem. Liq. 29 (1995) 43–58. https://doi.org/10.1080/00319109508030263.
[67] M.S. Turaeva, S.A. Kot, M.M. Urchukova, I.V. Murin, Effect of the Electrode Material on the Reduction of La3+ and Ce3+ in Fluoride-Conducting Solid Electrolytes, Russ. J. Electrochem. 41 (2005) 582–591. https://doi.org/10.1007/s11175-005-0110-3.
[68] C. Zhang, D. Rappleye, A. Nelson, S. Simpson, M. Simpson, Electroanalytical Measurements of Oxide Ions in Molten CaCl2 on W electrode, J. Electrochem. Soc. 168 (2021) 097502. https://doi.org/10.1149/1945-7111/ac208e.
[69] M. Goto, D. Ishii, Semidifferential electroanalysis, J. Electroanal. Chem. Interfacial Electrochem. 61 (1975) 361–365. https://doi.org/10.1016/S0022-0728(75)80237-3.
[70] P. Dalrymple-Alford, M. Goto, K.B. Oldham, Shapes of derivative neopolarograms, J. Electroanal. Chem. Interfacial Electrochem. 85 (1977) 1–15. https://doi.org/10.1016/S0022-0728(77)80148-4.
[71] P. Dalrymple-Alford, M. Goto, K.B. Oldham, Peak shapes in semidifferential electroanalysis, Anal. Chem. 49 (1977) 1390–1394. https://doi.org/10.1021/ac50017a025.
[72] M.M. Tylka, J.L. Willit, J. Prakash, M.A. Williamson, Application of Voltammetry for Quantitative Analysis of Actinides in Molten Salts, J. Electrochem. Soc. 162 (2015) H852–H859. https://doi.org/10.1149/2.0281512jes.